

# Tensor neural networks for high-dimensional Fokker-Planck equations

Taorui Wang\*    Zheyuan Hu<sup>†</sup>    Kenji Kawaguchi<sup>†</sup>    Zhongqiang Zhang\*  
 George Em Karniadakis<sup>‡</sup> §

April 9, 2024

## Abstract

We solve high-dimensional steady-state Fokker-Planck equations on the whole space by applying tensor neural networks. The tensor networks are a tensor product of one-dimensional feedforward networks or a linear combination of several selected radial basis functions. The use of tensor feedforward networks allows us to efficiently exploit auto-differentiation in major Python packages while using radial basis functions can fully avoid auto-differentiation, which is rather expensive in high dimensions. We then use the physics-informed neural networks and stochastic gradient descent methods to learn the tensor networks. One essential step is to determine a proper truncated bounded domain or numerical support for the Fokker-Planck equation. To better train the tensor radial basis function networks, we impose some constraints on parameters, which lead to relatively high accuracy. We demonstrate numerically that the tensor neural networks in physics-informed machine learning are efficient for steady-state Fokker-Planck equations from two to ten dimensions.

*Keywords:* physics-informed neural networks, training kernel methods, high-dimensional approximation, density estimation

## 1 Introduction

Fokker-Planck equations are often used to describe probability density functions for dynamical systems perturbed by random noise, such as in statistical mechanics, biology, finance, and engineering. Solutions to Fokker-Planck equations are often obtained numerically; see e.g. in [Risken]. However, numerical methods for Fokker-Planck equations often require to address the following issues: approximation in unbounded domains and high dimensions. Thus, solving the Fokker-Planck equation can be challenging with grid-based numerical methods such as finite difference or finite element methods, especially in high dimensions.

Instead of grid-based methods, mesh-free numerical methods via neural networks such as physics-informed neural networks [49] may be applied to alleviate these difficulties in high dimensions. The

---

\*Department of Mathematical Sciences, Worcester Polytechnic Institute, Worcester, MA 01609 USA (twang13@wpi.edu, zzhang7@wpi.edu)

<sup>†</sup>Department of Computer Science, National University of Singapore, Singapore, 119077 (e0792494@u.nus.edu, kenji@nus.edu.sg)

<sup>‡</sup>Division of Applied Mathematics, Brown University, Providence, RI 02912, USA (george.karniadakis@brown.edu)

<sup>§</sup>Advanced Computing, Mathematics and Data Division, Pacific Northwest National Laboratory, Richland, WA, United States

main idea is to formulate the problem of solving partial differential equations (PDEs) as solving optimization problems while using neural networks as approximate solutions. Some popular choices are using the L2-norm of the residuals of the underlying PDEs (known as physics-informed Neural networks, PINNs [49]) or using the variational formulation, e.g., [30] and [39]. The derivatives in the loss are usually computed via auto-differentiation and back-propagation for deep neural networks. The loss functions are realized by sampling random collocation/training points. This leads to discrete loss functions for optimization over the parameters of the deep neural networks, which are often trained/optimized with stochastic gradient methods such as ADAM methods [33]. This approach has been successfully applied to many problems; see e.g., in the reviews [16, 31] and many related works.

The challenges of machine learning algorithms for high-dimension PDEs lie in many aspects, such as 1) *effective loss functions*, 2) *computing derivatives inexpensively*, 3) *effective training points*, and 4) *efficient training methods*. These issues are somewhat addressed in the literature, see Section 2.1. However, some important issues have not yet been explored. For example, for high dimensional PDEs, solutions may be small in most regions where solutions are still meaningful. Resolving such small but meaningful scales can be challenging. A simple example is the computation of the density function  $(2\pi)^{-\frac{d}{2}} \exp(-\frac{|x|^2}{2})$ . When  $|x| = 1/2$  and  $d = 10$ , the function values are about  $10^{-4}$ . Another issue in high dimensional problems is the lack of effective benchmark problems/solutions to test. For example, in standard tests for high dimensional integration [17], the functions are usually tensor-product functions or composition of simple functions with a weighted summation of inputs or quadratic functions of the input arguments. To the best of our knowledge, the target solutions/functions considered in solving high-dimensional PDEs via networks are simple and most are radial basis functions. These benchmark problems effectively test the algorithms but do not address the approximation issues in high dimensions.

There have been a few works on machine learning algorithms for Fokker-Planck equations, see Section 2.2. However, in addition to the issues above, the following challenges have not been addressed for Fokker-Planck equations, including a) *finding effective numerical supports or picking the computational domains*; b) *the design of the networks for large approximation capacity*; and c) *numerical integration in high dimensions crucial for numerical probability density function, whose integral must be close to 1*.

In this work, we employ the framework of physics-informed neural networks for Fokker-Planck equations as in [3, 15, 62] using tensor neural networks. However, the loss function herein is different from these works. Specifically, we use the loss function (4), where the integral of the solution being 1 is implemented via normalization instead of penalization. Compared to [15, 62], where a large amount of data is generated from the Monte-Carlo simulations of stochastic differential equations (SDEs), we use only little data before the training. Specifically, we select numerical supports from a few simulated trajectories of corresponding SDEs and find this selection addresses the issue a) above in 6 dimensions. This step is crucial as numerical supports determine the computational domain and highly affect the number of training points and thus the computational cost.

To address the issue b), we use the tensor neural networks: tensor radial basis function networks and tensor feedforward networks for steady-state Fokker-Planck equations in high dimensions (from 2 to 10 dimensions). Both networks are universal approximations, i.e., they can approximate continuous functions on compact sets arbitrarily well; see Appendix A. The tensor feedforward neural networks have been proposed for low-dimensional problems, e.g., in [13, 58, 59, 63] but have not been tested in high dimensions. Also, tensor radial basis function networks have not been investigated for high dimensional PDEs, especially for Fokker-Planck equations.

The use of tensor radial basis function networks in high dimensions can be advantageous. We

can avoid auto-differentiation in computing the derivatives of each term in loss functions. In fact, due to the structure of tensor radial basis function networks, the derivatives in the spatial variables and the parameters of the networks are simple to compute and thus save huge storage required by the prevalent auto-differentiation Python packages. Compared to tensor feedforward neural networks, training tensor radial basis function networks is more demanding. We propose also an effective initialization and impose constraints for different parameters for the tensor radial basis function networks and provide a pragmatic approach for efficient approximations in high dimensions. Furthermore, we compare these two types of networks in Section 4.

The issue c) can be well accommodated by tensor radial basis function networks as it is straightforward to compute the integration. For tensor feedforward neural networks, we use accurate and reliable quadrature rules for numerical integration - Gauss quadrature is accurate for smooth integrands while Monte Carlo may be universal but less accurate.

In addition, we address the issue of approximation of complicated functions in high dimensions, which has not been investigated thoroughly in the literature. While the target solutions/functions in high dimensions are simple, e.g. linear or radial basis functions, our solutions are not Gaussian or Gaussian mixture, and they have complicated interactions among different coordinates and multiple modes. Here we assume that solutions are negligible outside of the numerical supports but involve non-trivial interactions among directions/arguments/dimensions. We observe that in high dimensions, the training results are sensitive to the numerical support; see Example 4.5 where smaller numerical supports are preferred in ten dimensions. We also introduce a metric for measuring the approximation errors in high dimensions while focusing on high-probability regions.

This paper is organized as follows. In Section 2, we summarize works on high-dimensional PDEs and those focusing on Fokker-Planck equations. We present in Section 3 the problem of interest and the methodology in this work. In Section 4, we present five examples in several dimensions. We also compare tensor radial basis function networks and tensor feedforward networks in the first three examples. We summarize our work in Section 5 and discuss some limitations of the work and possible directions to be addressed in the future.

## 2 Literature review

In this section, we review first some general issues and related literature in machine learning methods for high dimensional PDEs and then discuss specific problems in methods for Fokker-Planck equations. Here we do not intend to have a complete list of related works as it is almost impossible due to the fast development in literature. Instead, we focus on some fundamental issues of interest to our work.

### 2.1 General issues in high dimensions

Some challenges stated above for high dimensional problems have been addressed in the literature.

For effective loss function, we may use the combination of the learning approach and the probabilistic representation (e.g., Feynman-Kac) of the solutions, i.e., representation using solutions stochastic differential equations, see e.g. DeepBSDE [20, 21] and many works along this direction [7, 8, 6, 9, 11, 23, 26, 27, 29, 48, 64] and [16] for a review. We remark that this approach addresses only local approximations such as solutions at one or a few points and may require extensive computations for solutions in a large region.

For computing derivatives inexpensively, several approaches have been applied for feedforward neural networks:

- a) Randomized calculus for [22], by replacing the approximate solution and its derivatives with their stochastic approximation by Stein’s identity. The replacement leads to no auto-differentiation and no back-propagation for derivatives in physical variables. This methodology may be used in higher dimensions but is limited to no larger than 4 dimensions in [22].
- b) Tensor neural networks for low dimensional partial differential equations. Wang et al. [58, 59] propose tensor neural networks for solving Schrödinger equations. [13] applied the so-called separable PINNs for PDEs. In [63], a low-rank neural network is applied to solve PDEs. The networks therein are of the form  $\sum_{l=1}^r \bigotimes_{j=1}^d NN_j^l$  where  $NN_j^l$ ’s are neural networks of one dimension. In these papers, problems in up to four dimensions are considered. We will use tensor neural networks for higher dimensional problems.
- c) A random batch method in dimensionality has been developed in [24]. Therein, the computational cost of derivatives of feed-forward neural networks consists of computing the derivative in a few randomly picked dimensions and repeating the process.

As an alternative to feed-forward neural networks, radial basis function or more generally kernel function networks such as additive kernels or mixtures of kernels have been applied to accommodate the complex structures in the underlying problems and thus increase the capacity of the kernel approximations. For example, additive kernels are used to solve low-dimensional PDEs, e.g. in [42, 41, 52]. They are also widely used in machine learning algorithms, e.g., [5] in support vector machines. An extension of additive kernels is known as multiple kernels in multiple kernel learning where a linear or non-linear combination of base kernels is used. Many algorithms of multiple kernel learning for large-scale problems have been proposed to reduce computational complexity and memory usage, e.g., in [1, 28, 34, 43, 45, 50, 53, 56]. It has been shown recently that additive kernels can learn complex dynamics, e.g. [46, 19, 12, 61]. We remark that in this work we will use Adam methods instead of the algorithms in the above multiple kernel learning.

## 2.2 Solving Fokker-Planck equations with neural networks

The methods above may be applied to general PDEs and are not particularly designed for Fokker-Planck equations. Below we present a compact review of some recent works on numerical Fokker-Planck equations via neural networks.

The formulation of physics-informed neural networks for Fokker-Planck has been used, e.g., in [3, 15, 62]. Choices of loss functions other than the least-square formulation in physics-informed neural networks are also made. In [39], the loss function is not the  $L2$ -norm of residual of PDEs but a variational formulation as in [30]. Also, the high dimension equation is transformed into a system of finite dimensional ordinary differential equations in [39].

In addition to feedforward neural networks, generative models are also applied for PDEs with density solutions, especially for approximating density functions. See e.g., [10, 39, 55] for the use of flow-based networks, [4, 54] for Gaussian mixtures.

If observation data is available, data can be incorporated into loss functions. For example, the authors in [15, 62] use sampled solutions of the corresponding SDEs by Monte Carlo simulation as training points and also in data loss. For time-dependent Fokker-Planck equations, it is remarked in [36] that concentrating the training at the initial and the terminal time can improve the training efficiency. In [37, 38], the goal is to compute generalized potential via given data, i.e the logarithm of the invariant distribution for time-independent Fokker-Planck. The logarithmic transformation of the solution is also applied in [40] for time-dependent Fokker-Planck equations. In [40], the

long short-term memory model is used with physics-informed neural networks to solve the time-dependent Fokker-Planck equations. With a large amount of data generated by an SDE, [18] aims to find accurate density functions by first estimating the drift and diffusion coefficients of the SDE and then solving the Fokker-Planck equation with estimated coefficients.

Radial Basis Function (RBF) methods have been utilized to solve PDEs, as noted in [35]. Techniques such as Kansa’s approach, Hermite interpolation, and the Galerkin method have been utilized to implement these RBFs in solving the Fokker-Planck Equation, as detailed in [32] and [14]. Furthermore, [57] employs the RBF neural network, specifically using the Gaussian RBF function and normalization, to solve the steady-state Fokker-Planck equation. However, these works address only problems in low dimensions.

### 3 Problem and methodology

Consider the following Fokker-Planck equation

$$\mathcal{L}p = - \sum_i \frac{\partial}{\partial x_i} (f_i p)(x) + \frac{1}{2} \sum_{i,j} \frac{\partial^2}{\partial x_i \partial x_j} (D_{ij} p)(x) = 0, \quad x = (x_1, \dots, x_d) \in \mathbb{R}^d, \quad (1)$$

with  $\int_{\mathbb{R}^d} p(x) dx = 1, p \geq 0$ . We are limited to a class of Fokker-Planck equations, which serves as the unique invariant distribution of a stochastic differential equation. Here we refer [25] to interested readers for some theoretical consideration of steady-state Fokker-Planck equations.

In this work, we use tensor product networks of the following form

$$p_N(x; \theta) = \sum_{i=1}^N c_i \bigotimes_{j=1}^d k_{ij}(x_j; \theta_{i,j}) \quad x \in \mathbb{R}^d, k_{ij}(x_j) \geq 0, c_i \geq 0, \quad x_j \in \mathbb{R}. \quad (2)$$

Here ‘ $\otimes$ ’ refers to the tensor product and  $k_{ij} : \mathbb{R} \rightarrow \mathbb{R}^+ \cup \{0\}$  is a univariate function of  $x_j$ . We call  $N$  the rank of the tensor product networks. We use two types of neural networks for  $k_{ij}$ : either feedforward neural networks or radial basis function networks. When  $k_{ij}$ ’s are all radial basis function networks, each  $k_{ij}$  is an additive kernel, i.e., linear combination of radial basis functions (RBF) in the following form:

$$k_{ij} = \sum_{\ell=1}^m \alpha_{ij}^{(\ell)} k_{ij}^{(\ell)} \left( \left| \frac{x_j - s_{ij}^{(\ell)}}{h_{ij}^{(\ell)}} \right| \right), \quad \alpha_{ij}^{(\ell)} \geq 0, \sum_{\ell=1}^m \alpha_{ij}^{(\ell)} = 1. \quad (3)$$

Here the radial basis function or kernel  $k_{ij}^{(\ell)}$  has two families of parameters: shifts/anchor points  $s_{ij}^{(\ell)}$ , and bandwidth/scaling factors  $h_{ij}^{(\ell)}$ . All the parameters in the RBFs are trainable, We call this tensor network as *Tensor Radial Basis Function Networks* (abbreviated as TRBFN). When  $k_{ij}$ ’s are feed-forward neural networks, we set  $c_i = 1$  and use the activation function *tanh* for all inner layers and the softplus function for the last layer of  $k_{ij}$ . We call this network *Tensor Feed-Forward Network* (abbreviated as TFFN).

#### 3.1 Loss function

In the loss function, we incorporate the residual of the Fokker-Planck equation (1) and the integration of the approximated solution being 1 while the non-negativity of the solution can be

accommodated by applying a non-negative activation function in the last layers of 1D feedforward networks or using non-negative radial basis functions. At the continuous level, we use the following loss function:

$$\int_{\Omega} \left( \mathcal{L} \frac{p_N(x; \theta)}{\int_{\Omega} p_N(y; \theta) dy} \right)^2 dx. \quad (4)$$

where  $\Omega$  is a large and bounded domain in  $\mathbb{R}^d$  such that  $1 - \int_{\Omega} p^* dx$  is sufficiently small and  $p^*$  is the exact solution. We note that the constraint of the integration being 1 is imposed through the normalization of the numerical solution  $p_N$ . We also impose the zero Dirichlet boundary condition on  $\partial\Omega$ , which will be discussed in detail in Section 3.2.

In this work, we take  $\Omega$  as a hypercube  $\bigotimes_{j=1}^d [O_j - r_j, O_j + r_j]$  such that we can integrate our tensor product on this hypercube in a simple way:

$$\int_{\Omega} p_N(x; \theta) dx = \sum_{i=1}^N c_i \left( \prod_{j=1}^d \int_{[O_j - r_j, O_j + r_j]} k_{ij}(x_j; \theta_{ij}) dx \right).$$

To determine  $O_j$ , we apply the Euler scheme for the SDE corresponding to the underlying Fokker-Planck equation to obtain a few simulated trajectories. Denote by  $\Xi$  the set of trajectory points at the terminal time. We choose  $O = (O_1, O_2, \dots, O_d)$  as the center of the set  $\Xi$ . A simple way is to set the numerical support by picking  $r_j = B > 0$  and  $\Omega = \bigotimes_{j=1}^d [O_j - B, O_j + B] \supset \Xi$  as an *initial numerical support*. If the initial numerical support turns out to be of a large volume, we may use a smaller numerical support as follows. To find  $r_j$ , we first train a tensor radial basis network with  $r = B$  with a certain number of epochs and denote this tensor network as  $p_N$ . We then want to find a small  $r^* < B$ , which corresponds to region  $\Omega^* = [O_j - r^*, O_j + r^*]$  and  $\Omega^*$  can still be denoted as  $\Omega$  if no confusion arises. We desire that  $\int_{\Omega^*} p_N dx$  is greater than a threshold,  $\vartheta$ . Since  $\int_{\Omega^*} p_N dx$  can be computed exactly, finding  $r^*$  is solving a constrained optimization problem:

$$\text{Find the minimum of } : r^* \in (0, B), \text{ such that } r_j = r^*, j = 1, \dots, d, \text{ and } \int_{\Omega^*} p_N dx > \vartheta.$$

We solve this problem approximately as follows. Starting with  $r^* = B$ , we set  $r^* = lr^*$  ( $l \in [0.9, 0.97]$ ) and check if  $\int_{\Omega^*} p_N dx > \vartheta$ . This process can be repeated several times to find some  $r^*$  in this process and we then set the numerical support as  $\Omega = \bigotimes_{j=1}^d [O_j - r^*, O_j + r^*]$ , which we call *refined numerical support*.

### 3.2 Training settings

In this section, we present the settings in training. Both TRBFN and TFFN are implemented in the Python programming language using the JAX library. We use the ADAM methods from LION (<https://github.com/lucidrains/lion-pytorch>) for training both networks with a polynomial schedule. The number of epochs is  $10^5$  unless otherwise stated.

For the tensor feedforward networks (TFFN), we use the following setting. We use the piecewise Gauss-Legendre quadrature rule to compute the integral  $\int_{[O_j - r_j, O_j + r_j]} k_{ij}(x_j, \theta_{ij}) dx_j$  and then compute  $\int_{\Omega} p_N(x; \theta) dx$ . Specifically, we split  $[O_j - r_j, O_j + r_j]$  into  $M = 16$  subintervals and use 16 Gauss-Legendre quadrature points with corresponding weights in each subinterval.

To ensure that the value of TFFN is close to 0 at  $\partial\Omega$ , we multiply TFFN by the function  $\prod_{j=1}^d ((1 - x_j^2/r_j^2)^3)_+$ . We observe that we need double precision (float64) to obtain meaningful training results. We apply Xavier Glorot's initialization to each feedforward neural network  $k_{ij}$ .

The training batch size is 4096 for TFFN unless otherwise stated. We conduct all experiments of TFFN on an NVIDIA A100 GPU with 80 GB memory.

For the tensor radial basis function networks, we let  $\sum_{i=1}^N c_i = 1$  and the integration of all kernels  $k_{ij}$  over  $[O_j - r_j, O_j + r_j]$  being 1. We use a large  $N$  in (2) and a small  $m$  in (3).  $s_{ij}^{(\ell)}$  in (3) are constrained by  $|s_{ij}^{(\ell)} - O_j| < r_j$  and  $h_{ij}^{(\ell)}$  in (3) is constrained by:

$$|h_{ij}^{(\ell)}| < |r_j - |s_{ij}^{(\ell)} - O_j||. \quad (5)$$

The constraints of  $s_{ij}^{(\ell)}$  and  $h_{ij}^{(\ell)}$  are imposed through penalization as extra loss terms in Equation (4):

$$\sum_{i,j,\ell} ((|s_{ij}^{(\ell)} - O_j| - r_j)_+ + (|h_{ij}^{(\ell)}| - (|r_j - |s_{ij}^{(\ell)} - O_j||))_+).$$

We also add a penalty term to ensure TRBFN is close to 0 at  $\partial\Omega$  if  $k_{ij}$  includes RBFs without compact support. The following term is added to the loss function (4) as penalty:

$$\sum_{i,j} ((k_{ij}(O_j + r_j) + k_{ij}(O_j - r_j))). \quad (6)$$

We note that including one compactly supported kernel in  $k_{ij}$  can help to enable TRBFN to be close to 0 at  $\partial\Omega$ . The effect of penalty term is discussed in Example 4.5 of Section 4. We use the following radial basis functions in (3): Gaussian  $\exp(-|x|^2)$ , Inverse multi-quadratic  $((1+|x|^2)^{-2.5})$ , and Wendland's function (compactly supported)  $((1 - |x|)_+)^3(3|x| + 1)$ .

We initialize all  $s_{ij}^{(\ell)}$  constrained within  $[O_j - r_j, O_j + r_j]$  and normally distributed with mean  $O_j$  and standard error  $\sqrt{r_j}$ . Initially, bandwidths or scaling factors  $h_{ij}^{(\ell)}$  are set to be greater than  $0.9r_j$ . We initialize  $c_1 = \dots = c_N = 1/N$  and  $\alpha_{ij}^{(1)} = \dots = \alpha_{ij}^{(m)} = 1/m$ . We observe that the performances of TRBFN are similar under double precision (float64) and single precision (float32). The training batch size is 5000 for TRBFN unless otherwise stated. We conduct all experiments of TRBFN on an NVIDIA A100 GPU with 40 GB memory.

**Remark 3.1.** Increasing the number of  $N$  and  $m$  can increase TRBFN's approximation capacity. But increasing the number of  $N$  seems more significant than increasing the number of  $m$ . For our experiments in Example 4.1, we found that increasing  $N$  with a small number of  $m$  ( $m < 10$ ) can produce smaller losses and more accurate solutions than increasing  $m$  with a small number of  $N$  ( $N < 10$ ). Note that the number of parameters of TRBFN is at the order  $3Ndm$ . We thus choose a large  $N$  and a small  $m$  for TRBFN in Section 4. For TFFN, we use a relatively small  $N$  while we use the size of the one-dimensional feedforward neural networks to control the number of parameters. For example, if we use a networks with  $l + 1$  hidden layers and the architecture  $[1, w, \dots, w, 1]$ , the number of parameters is at the order of  $Ndlw^2$ . In practical implementation, we need a balance between the rank  $N$  and the number of radial basis functions or the size of feedforward neural networks, due to the tensor implementation of prevalent Python packages.

## 4 Numerical results

In this section, we consider the equation (1) with the following drift

$$f(x) = -\frac{1}{2}D(x)\nabla H(x) + g(x), \quad g_i(x) = \sum_{j=1}^d \frac{\partial}{\partial x_j} \left( \frac{1}{2} D_{ij}(x) \right). \quad (7)$$

Then the solution to (1) reads

$$p(x) = \frac{1}{\int_{\mathbb{R}^d} \exp(-H(x)) dx} \exp(-H(x)). \quad (8)$$

We remark that the methodology in this work can be applied to the equation (1) but the specific drift allows us to have a baseline solution to compare with.

To evaluate the numerical results, we use the following relative error

$$\frac{1}{n} \sum_{i=1}^n \left| \frac{p^*(x_i) - p_N(x_i)}{p^*(x_i)} \right|, \quad x_i \in \Gamma_\varepsilon = \{x \in \Gamma | p^*(x) > \varepsilon\}. \quad (9)$$

Here  $p^*(x)$  represents the exact solution and  $p_N(x)$  is the numerical solution obtained from tensor neural networks. Also,  $\Gamma \subset \mathbb{R}^d$  is a set of interest and  $\varepsilon > 0$  and is specified in each example. The testing points  $x_i$ 's are uniformly sampled from the region  $\Gamma$  of interest unless otherwise specified.

We test TRBFN on five examples and of steady-state Fokker-Planck equations. We have experimented with several choices of different RBFs in (3). For simplicity, we denote by TRBFN( $N$ ,  $m$ ) the tensor radial basis function neural networks with the rank  $N$  in (2) and the number of basis  $m$  in (3). We test TFFN on first three examples. We also denote by TFFN( $N$ ,  $\cdot$ ) the tensor feedforward neural networks with the rank  $N$  in (2) and the architecture of the 1D feedforward neural network “.”.

**Example 4.1** (2D Ring potential). Consider the steady Fokker-Planck equation (1) with the following drift  $f$  in (7) using  $H(x) = 2(x_1^2 + x_2^2 - 1)^2$ , and diffusion  $D = 2I_{2 \times 2}$ . This example was used in [62]. The potential function  $H(x)$  has the level curve  $x_1^2 + x_2^2 = 1$ , where the exact solution (the density function) reaches its mode.

In this example, we use the numerical support  $\Omega = [-3, 3]^2$ , which contains 100 trajectories of the corresponding SDE solver. First, we test the tensor radial basis function networks. The radial basis function  $k_{ij}$  in (3) for TRBFN only contains the Wendland kernel functions. We also test other combinations of various kernels and obtain similar results and thus do not present them. We use TRBFN(5, 720) and TRBFN(1000, 3). For both networks, we plot the history of loss functions versus training epochs in Figure 1. We observe that the loss functions from TRBFN(1000, 3) are much smaller than those for TRBFN(5, 720) around  $10^5$ -th epochs:  $10^{-4}$  vs  $10^{-2}$ . The smaller loss functions suggest better approximation, which is observed in Table 1. In the table, we present the relative errors defined in (9), where the points  $x_i$  are from  $10^5$  points sampled from Gaussian variables  $\mathcal{N}(0.0, 0.5138I_{2 \times 2})$  and we exclude the points that are not in  $\Gamma_\varepsilon$  with  $\varepsilon = 10^{-2}, 5 \times 10^{-2}, 10^{-1}$ . From Table 1, we observe that using TRBFN(1000, 3) achieves accuracy that is at least one order of magnitude higher than using TRBFN(5, 720). This suggests that the large rank ( $N = 1000$ ) in the tensor radial basis function networks results in larger approximation capability than a small rank ( $N = 5$ ).

Second, we also present results in Table 1 from tensor feedforward neural networks. We observe that for TFFN, it is also true that a larger rank  $N$  leads to better accuracy. For example, TFFN(160, [1, 8, 8, 1]) leads to smaller relative errors than TFFN(64, [1 8 8 1]). While compared with TRBFN, TFFN achieves the same magnitude of accuracy under rank  $N = 5$ , around  $10^5$  epochs. When we run more epochs with TFFN, e.g.,  $1 \times 10^6$ , we observe that the average relative error for TFFN(10, [1 32 32 32 1]) is around 0.1% on the region  $\Gamma_{10^{-2}}$ .



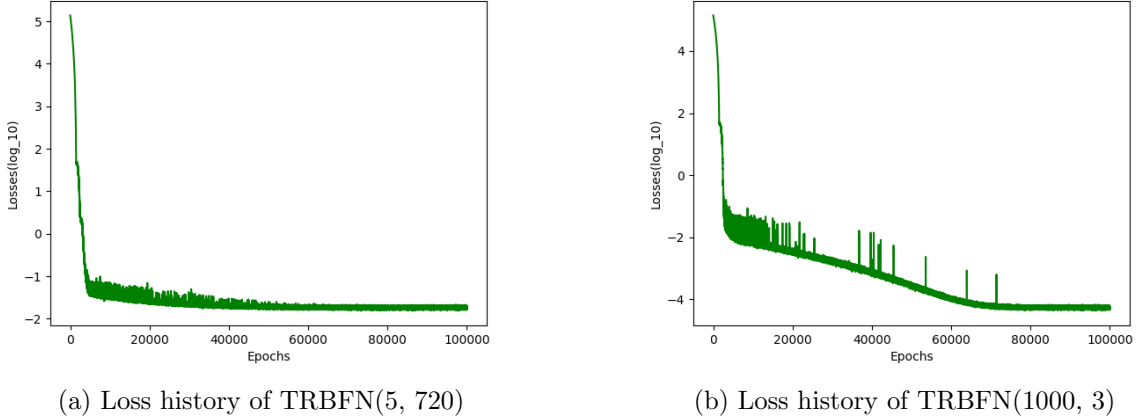


Figure 1: Example 4.1: history of loss function. In TRBFN, we use the Wendland kernel.

model	# parameters (est.)	density region/error		
		$\Gamma_{1 \times 10^{-2}}$	$\Gamma_{5 \times 10^{-2}}$	$\Gamma_{1 \times 10^{-1}}$
TRBFN(1000,3)	19000	0.0001	0.0001	0.0001
TRBFN(5,720)	21605	0.0041	0.0031	0.0022
TFFN(5,[1 32 32 32 1])	21120	0.0054	0.0046	0.0045
TFFN(64,[1 8 8 1])	10240	0.0036	0.0031	0.0027
TFFN(160,[1 8 8 1])	25600	0.0020	0.0015	0.001
TFFN(10,[1 32 32 32 1])	42240	0.0012	0.0011	0.0009
# of test points $n$		89164	76013	54920

Table 1: Example 4.1: average relative errors (9) for different tensor neural networks. Here we sample  $10^5$  points from  $\mathcal{N}(0,0,0.5138I_{2 \times 2})$  and pick the points  $x_i$ 's located in  $\Gamma_\varepsilon = \{x \in \Gamma = \mathbb{R}^2, p^*(x) > \varepsilon\}$ . All networks are trained with  $10^5$  epochs, except for TFFN(10, [1 32 32 32 1]), where we use  $10^6$  epochs.

**Example 4.2** (4D example with a single mode). Consider the drift (7) with the following potential function and the diffusion

$$H(x) = 3((x_1^4 - x_2)^2 + 2x_2^2) + 2(x_3^2 - 0.3(x_3x_4) + x_4^2),$$

$$D = 2 \begin{bmatrix} 1 & 0 & 0 & 0 \\ 0 & 1 & 0 & 0 \\ 0 & 0 & 1.0 + V(x_3, x_4) & V(x_3, x_4) \\ 0 & 0 & V(x_3, x_4) & 1.0 + V(x_3, x_4) \end{bmatrix}, \quad V(x_3, x_4) = 0.1x_3^2x_4^2.$$

The exact solution  $p^*$  in Example 4.2 has a mode at  $(0, 0, 0, 0)$  while  $H(x)$  exhibits complex interactions between  $x_1$  and  $x_2$ , and between  $x_3$  and  $x_4$ . Specifically, the component  $(x_1^4 - x_2)^2 + 2x_2^2$  results in a high probability region focused around the line  $x_1 = x_2$ . Moreover, large gradients arise along the line  $x_1 = x_2$  near the origin. The components involving  $x_3$  and  $x_4$  in  $H(x)$  leads to the density function concentrated around the point  $(0, 0, 0, 0)$ .

By the procedure described in Section 3.1, we run 100 trajectories of the corresponding SDE and obtain an initial numerical support  $[-2.6, 2.6]^4$ .

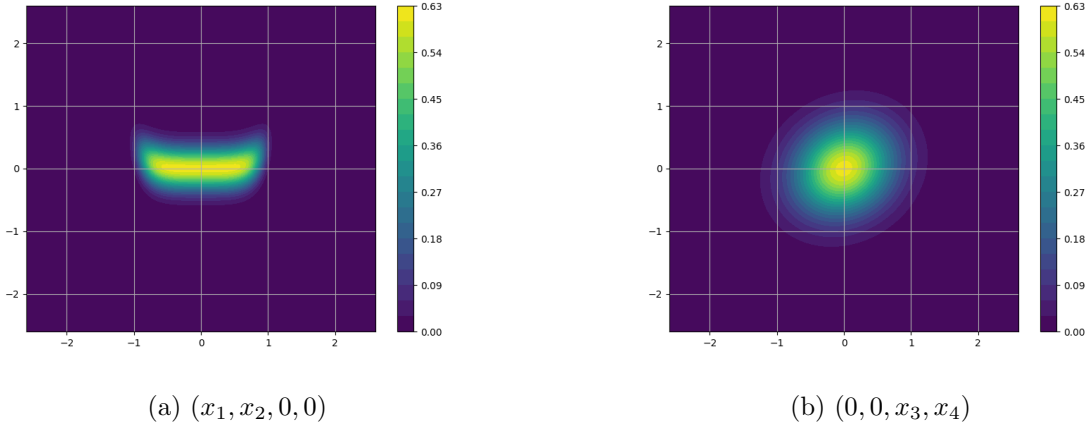


Figure 2: Contour maps of projections of the exact solution  $p^*(x)$  in Example 4.2

First, we test TRBFN and TFFN on  $[-2.6, 2.6]^4$ . The radial basis function  $k_{ij}$  within TRBFN only contains the family of Wendland kernel functions. We report in Table 2 the average relative errors. For example, all the relative average errors from TRBFN is less than 1% on  $\Gamma_{10^{-2}}, \Gamma_{5 \times 10^{-2}}, \Gamma_{10^{-1}}$ , except TRBFN (64,27) on  $\Gamma_{10^{-2}}$ . Comparing results in Table 2 among TRBFNs, we conclude that a large rank and a small  $m$  may lead to better accuracy. For results from TFFN in Table 2, a larger rank  $N$  with the same size of feedforward neural networks leads to accuracy of one order of magnitude higher.

Next, we use a smaller support  $[-2, 2]^4$  which is the refined numerical support and obtained through the procedure in Section 3.1, by setting  $\vartheta = 0.98$  such that the integration of the trained network  $TRBFN(1000, 3)$  over  $[-2, 2]^4$  is larger than  $\vartheta$ . We also report in Table 2 the average relative errors for TFFN(64, [1 8 8 1]) and TFFN(128, [1 8 8 1]) trained on the numerical support  $[-2, 2]^4$ . The accuracy is improved for both TFFNs, especially for TFFN(64, [1 8 8 1]). Compared with results from the numerical support  $[-2.6, 2.6]^4$ , we observe that the smaller support leads to better accuracy for TFFN.

model	support $\Omega$	# parameters (est.)	density region/error		
			$\Gamma_{1 \times 10^{-2}}$	$\Gamma_{5 \times 10^{-2}}$	$\Gamma_{1 \times 10^{-1}}$
TRBFN(1000, 3)	$[-2.6, 2.6]^4$	37000	0.0054	0.0030	0.0019
TRBFN(64, 27)	$[-2.6, 2.6]^4$	20800	0.0152	0.0085	0.0055
TRBFN(128, 27)	$[-2.6, 2.6]^4$	41600	0.0088	0.0049	0.0032
TFFN(64, [1 8 8 1])	$[-2.6, 2.6]^4$	20480	0.1797	0.1311	0.1116
TFFN(128, [1 8 8 1])	$[-2.6, 2.6]^4$	40960	0.0600	0.0390	0.0297
TFFN(64, [1 8 8 1])	$[-2, 2]^4$	20480	0.0302	0.0184	0.0130
TFFN(128, [1 8 8 1])	$[-2, 2]^4$	40960	0.0317	0.0194	0.0135
# of test points $n$			48572	26693	17296

Table 2: Example 4.2: average relative errors (9) for different tensor neural networks. All  $1 \times 10^5$  test points  $x_i$ 's are sampled uniformly from  $\Gamma = [-1, 1]^4$ .

**Example 4.3** (6D unimode example). Consider the drift (7) with the following potential function  $H(x) = 3((x_1^4 - x_2)^2 + 2x_2^2 + (x_3^4 - x_4)^2 + 2x_4^2 + (x_5^4 - x_6)^2 + 2x_6^2)$  and the diffusion  $D = 2I_{6 \times 6}$ .

In Example 4.3, the potential  $H(x)$  has three specific terms of the form  $(x_i^4 - x_{i+1})^2$ ,  $i = 1, 3, 5$ . The density function is more concentrated and has steeper gradients in regions of high density compared to Example 4.2 of four dimensions.

The integration of the exact density is approximately 1 on  $[-1.6, 1.6]^6$  (with error  $10^{-6}$ ) and is approximately 0.944 on  $[-0.95, 0.95]^6$ . In this example, The training batch size is 12000 for TRBFN and 8192 for TFFN.

By the procedure described in Section 3.1, we run 100 trajectories of the corresponding SDE and obtain the initial numerical support  $[-1.6, 1.6]^6$ . On the support  $[-1.6, 1.6]^6$ , we first test this example with TRBFN(800, 3), where the Wendland kernel functions are used. We obtain a smaller support  $[-1.2, 1.2]^6$  by the procedure of finding a refined numerical support in Section 3.1, by setting the threshold  $\vartheta = 0.95$  with the trained TRBFN(800, 3). We test TFFN on  $[-1.2, 1.2]^6$ . We report the relative average errors in Table 3 for TFFN and TRBFN. While both networks can capture the key features of the exact solution, TRBFN admits smaller relative errors over regions present in the table. For TFFN, we observe that a larger rank  $N$  leads to smaller relative average errors, on the same support  $[-1.2, 1.2]^6$ . With a relatively small rank,  $N = 20$ , we observe that deeper and wider neural networks give better results on the same support.

model	support $\Omega$	# parameters (est.)	density region/error		
			$\Gamma_{5 \times 10^{-2}}$	$\Gamma_{2.5 \times 10^{-1}}$	$\Gamma_{5 \times 10^{-1}}$
TRBFN(800, 3)	$[-1.6, 1.6]^6$	44000	0.0561	0.0334	0.0259
TFFN(10, [1 32 32 32 1])	$[-1.2, 1.2]^6$	126720	0.1855	0.1132	0.0894
TFFN(20, [1 32 32 32 1])	$[-1.2, 1.2]^6$	253440	0.1001	0.0602	0.0479
TFFN(128, [1 8 8 1])	$[-1.2, 1.2]^6$	61440	0.3762	0.2646	0.2116
TFFN(20, [1 8 8 8 1])	$[-1.2, 1.2]^6$	17280	0.2763	0.1817	0.1427
# of test points $n$			34705	7796	1926

Table 3: Example 4.3: average relative errors (9) for different tensor neural networks. All  $5 \times 10^5$  test points  $x_i$ 's are sampled uniformly from  $\Gamma = [-1, 1]^6$ .

Those results from Examples 4.2 and 4.3 demonstrate the effectiveness of TRBFN and TFFN. However, the exact solutions in Examples 4.2 and 4.3 have one mode. In the next example, Example 4.4, we present a density function with multiple modes.

**Example 4.4** (6D with a solution with multiple modes). Consider the drift (7) with the following potential function and the diffusion

$$H = 2(x_1^2 + x_2^2 + x_3^2 + 0.5(x_1x_2 + x_1x_3 + x_2x_3)) - \ln(x_1^2 + 0.02) - \ln(x_2^2 + 0.02) \\ + 0.5(x_4^2 + x_5^2 + x_6^2 + 0.2(x_4x_5 + x_4x_6 + x_5x_6)), \quad D = 2I_{6 \times 6}.$$

The potential function  $H(x)$  in Example 4.4 has three way interactions: interaction among  $(x_1, x_2, x_3)$  and interaction among  $(x_4, x_5, x_6)$ . The density function has four modes and each mode is not close to the rest. In this example, the training batch size is 20000.

By the procedure described in Section 3.1, we obtain an initial numerical support  $[-5.5, 5.5]^6$ . Consequently, the solution on most of the region  $\Omega$  is very small and the loss functions oscillate with epochs; see Figure 4 where we use the tensor radial basis function network TRBFN(800, 3).

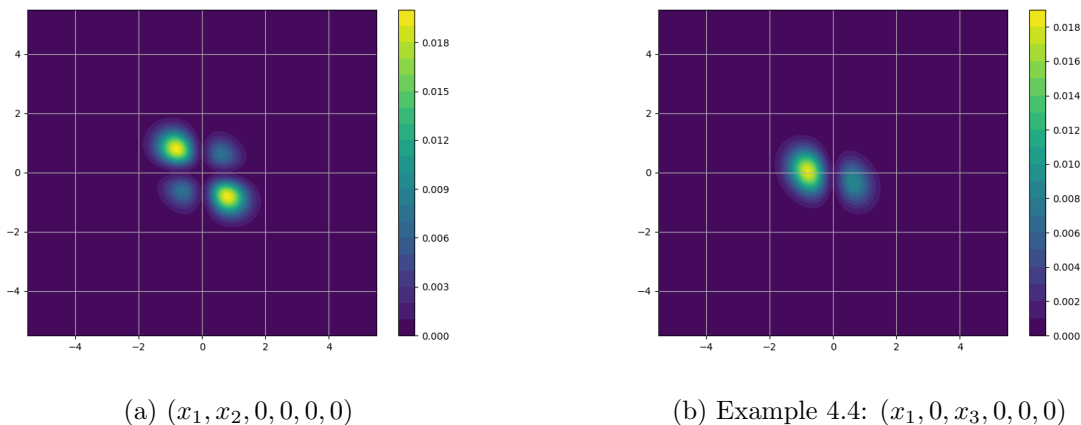


Figure 3: Contour maps of projections of the exact solution in Example 4.4

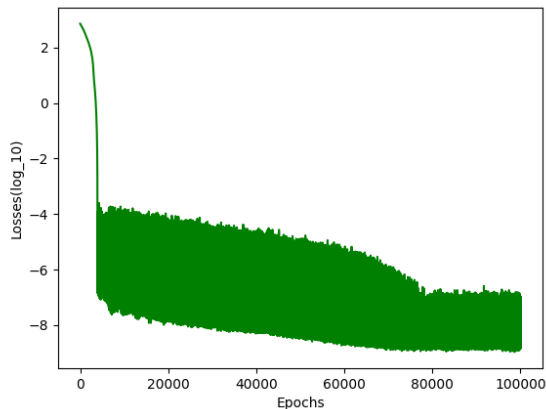


Figure 4: Example 4.4: Loss history, TRBFN(800, 3).

We first use the numerical support  $\Omega = [-5.5, 5.5]^6$ . We observe in Table 4 that the relative errors within different density regions are under 50%. We present the contour map of projections of the numerical solution in Figure 5 and observe that the numerical solution captures the modes of the exact solution.

Next, we refine the numerical support as described in Section 3.1. With the trained TRBFN(800, 3), we obtain  $[-4.35, 4.35]^6$  such that the integral of the TRBFN over the region is larger than the threshold  $\vartheta = 0.93$ . Then the numerical support is refined to be  $\Omega = [-4.35, 4.35]^6$ . We apply TRBFN(800, 3). In Table 5, we report the average relative error, which is less than 10% in the region  $\Gamma_{10^{-3}}$  and is less than 15% in  $\Gamma_{2 \times 10^{-4}}$ .

**Example 4.5** (10D Fokker-Planck with a multi-modal solution). Consider the drift (7) with the following potential function and the diffusion

$$H = 2.5(x_1^2 + x_2^2 + x_3^2 + 0.1(x_1x_2 + x_1x_3 + x_2x_3)) + 2.0(x_4^2 + x_5^2 + x_6^2 + 0.2(x_4x_5 + x_4x_6 + x_5x_6)) \\ + 3.0(x_7^2 + x_8^2 - 0.01(x_7x_8)) + 3.0(x_9^2 + x_{10}^2 - 0.01(x_9x_{10})) - \ln(2x_9^2 + 0.02), \quad D = 2I_{10 \times 10}.$$

In this example 4.5, the variables  $(x_1, x_2, x_3)$ ,  $(x_4, x_5, x_6)$ ,  $(x_7, x_8)$  and  $(x_9, x_{10})$  have distinct interactions and the exact solution has two modes. The density function is highly concentrated around

	density region/error		
	$\Gamma_{2 \times 10^{-4}}$	$\Gamma_{10^{-3}}$	$\Gamma_{5 \times 10^{-3}}$
TRBFN(800, 3)	0.4239	0.4508	0.487
# of test points $n$	91712	26334	2121

Table 4: Example 4.4: average relative errors (9) for TRBFN(800, 3) trained on  $\Omega = [-5.5, 5.5]^6$ . All  $5 \times 10^5$  test points  $x_i$ 's are sampled uniformly from  $\Gamma = [-2, 2]^6$ . The number of parameters of TRBFN(800, 3) is 44000 (est.).

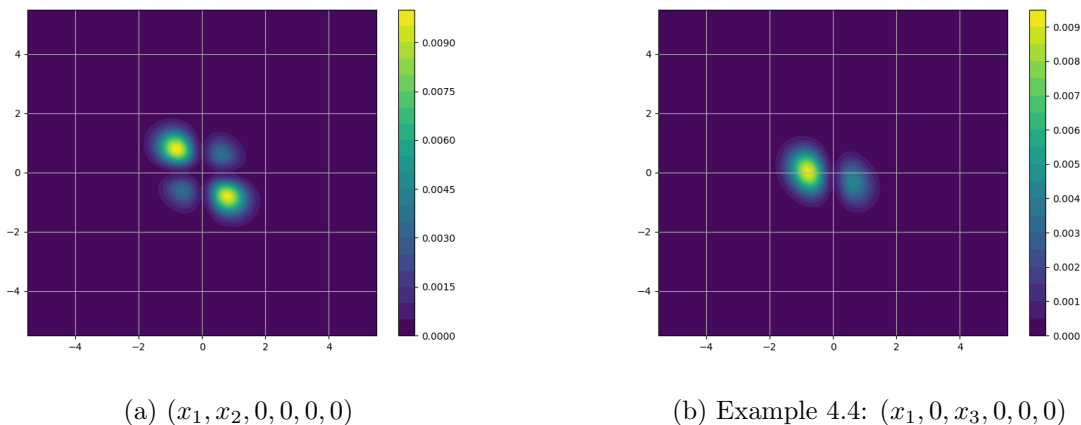


Figure 5: Contour maps of projections of the numerical solution in Example 4.4

model	density region/error		
	$\Gamma_{2 \times 10^{-4}}$	$\Gamma_{10^{-3}}$	$\Gamma_{5 \times 10^{-3}}$
TRBFN(800, 3)	0.1234	0.0826	0.0564
# of test points $n$	91712	26334	2121

Table 5: Example 4.4: average relative errors (9) for TRBFN(800, 3) trained on  $\Omega = [-4.35, 4.35]^6$ . All  $5 \times 10^5$  test points  $x_i$ 's are sampled uniformly from  $\Gamma = [-2, 2]^6$ . The number of parameters of TRBFN(800, 3) is 44000(est.)

two modes.

We test TRBFN only. As described in Section 3.1, we run 100 trajectories of the corresponding SDE and obtain the numerical support  $\Omega = [-2.5, 2.5]^{10}$ . We use TRBFN(1000,3) whose  $k_{ij}$  only contains Wendland kernel functions. We observe in Table 6 that the average relative errors are more than 95%. We then choose a smaller support  $\Omega_1 = [-1.8, 1.8]^{10}$ <sup>1</sup> such that  $\int_{\Omega_1} p^* dx \approx \int_{\Omega_1} \exp(-H(x)) dx / \int_{[-5,5]^{10}} \exp(-H(x)) dx \approx 0.9985$ . We observe that the integral of  $p^*$  over  $\Omega$  is approximately  $\int_{\Omega} \exp(-H(x)) dx / \int_{[5,5]^{10}} \exp(-H(x)) \approx 0.9999$ . This means that the density function on the region outside  $[-1.8, 1.8]^{10}$  is extremely small and contributes little while results from training on  $[-2.5, 2.5]^{10}$  are deteriorated by these small scales. With the smaller support, we observe that the average relative errors are drastically improved to be less than 8%.

We then use the numerical support  $[-1.8, 1.8]^{10}$  only and explore the effects of radial basis functions of different kinds in  $k_{ij}$  in (3). We test two TRBFN(1000, 3): (1)  $k_{ij}$  only contains the Wendland kernel function for all  $i, j$ , denoted as TRBFN(1000, 3)(w); (2)  $k_{ij}$  contains two Wendland's kernel functions and one inverse-quadratic function for all  $i, j$ , denoted as TRBFN(1000, 3)(wi). We test TRBFN(1000, 3)(wi) with and without adding penalty term (6) in Section 3.2.

The results in Table 7 suggest that TRBFN(1000, 3)(w) and TRBFN(1000, 3)(wi) capture the two modes of the exact solution. However, on the region  $\Gamma_{\epsilon > 10^{-3}}$ , the average relative error of the result of TRBFN(1000, 3)(wi) without adding penalty term (6) is 0.3490, which is much larger than 0.0595, the average relative error achieved by TRBFN(1000, 3)(w). The large error is because

<sup>1</sup>In this example, the refinement procedure in Section 3.1 does not work well as the TRBFN is inaccurate when trained on  $\Omega$ .

model	# parameters(est.)	Support $\Omega$	density region/error		
			$\Gamma_{10^{-3}}$	$\Gamma_{10^{-2}}$	$\Gamma_{10^{-1}}$
TRBFN(1000, 3)(w)	91000	$[-2.5, 2.5]^{10}$	0.9517	0.9551	0.9581
TRBFN(1000, 3)(w)	91000	$[-1.8, 1.8]^{10}$	0.0595	0.0643	0.0675
# of test points $n$			390830	96024	211

Table 6: Example 4.5: average relative errors (9) for TRBFN. All  $5 \times 10^5$  test points  $x_i$ 's are sampled uniformly from  $\Gamma = [-0.7, 0.7]^{10}$ . The numerical support is  $\Omega = [-2.5, 2.5]^{10}$ .  $k_{ij}$  only contains Wendland kernel functions

the numerical solution from TRBFN(1000, 3)(wi) at the boundary of the numerical support is not close to zero while TRBFN(1000,3)(w) is very close to zero at the boundary due to the compact support of the Wendland kernel function. When we impose vanishing boundary conditions for TRBFN(1000, 3)(wi) via penalization (6) as in Section 3.2, the accuracy is much improved and is comparable with TRBFN(1000, 3)(w).

model	# parameters(est.)	vanishing at $\partial\Omega$	density region/error		
			$\Gamma_{10^{-3}}$	$\Gamma_{10^{-2}}$	$\Gamma_{10^{-1}}$
TRBFN(1000, 3)(w)	91000	implicitly	0.0595	0.0643	0.0675
TRBFN(1000, 3)(wi)	91000	No	0.3490	0.3583	0.3702
TRBFN(1000, 3)(wi)	91000	explicitly	0.0705	0.0687	0.0755
# of test points $n$			390830	96024	211

Table 7: Example 4.5: average relative errors (9) for TRBFN trained on  $\Omega = [-1.8, 1.8]^{10}$ . All  $5 \times 10^5$  test points  $x_i$ 's are sampled uniformly from  $\Gamma = [-0.7, 0.7]^{10}$ .

## 5 Summary and discussion

We have investigated tensor radial basis function networks and tensor-feedforward neural networks for steady-state Fokker-Planck equations in high dimensions. We first designed a simple procedure for estimating efficient numerical supports and then applied these two types of networks for the equations over the numerical supports. For tensor radial basis functions, we imposed conditions to control the parameters in each radial basis function for better approximations. The radial basis functions allowed us to find the exact derivatives and integration over numerical support and thus significantly reduce storage requirements from auto-differentiation in major Python packages. The tensor feedforward networks are straightforward to implement but are more sensitive to numerical supports even in six or less dimensions. We presented several examples to illustrate the feasibility and accuracy of both tensor networks.

There are also some limitations of the current methodology. First, we use a hypercube as numerical support while for Fokker-Planck equations the numerical support may be large when the density function decay slowly or contains separated regions. Also, the efficiency is sensitive to the choice of numerical support as it may require more training points in a large support. Second, the choice of the kernels is somewhat arbitrary. More kernel functions of different kind may be employed for larger approximation capacity; see e.g. [19] and consequent works. Third, we imposed some

constraints on the parameters in radial basis functions, which are general but still are problem-dependent. An alternative approach is to use an alternating direction method in training these networks and apply a cross-validation strategy to determine when to stop computation, such as in [2, 47, 60]. We leave these issues for future study.

The methodology in this work may be combined with DeepBSDE or other methods for better accuracy, where an accurate solution is desired at a few points in the high-probability regions. For example, we may run tensor neural networks to obtain an estimate of high probability region and then compute the solution at the points of interest with DeepBSDE.

## Declaration of competing interest

The authors declare that they have no known competing financial interests or personal relationships that could have appeared to influence the work reported in this paper.

## Data availability

The code and data generated during and/or analysed during the current study will be available upon publication.

## Acknowledgement

We would like to thank Professor Houman Owhadi for helpful discussions and for providing valuable references. ZZ was partially supported by AFOSR under award number FA9550-20-1-0056. GK acknowledges support by the DOE SEA-CROGS project (DE-SC0023191) and the MURI-AFOSR project (FA9550-20-1-0358), and the ONR Vannevar Bush Faculty Fellowship (N00014-22-1-2795). This research of ZH and KK is partially supported by the National Research Foundation Singapore under the AI Singapore Programme (AISG Award No: AISG2-TC-2023-010-SGIL) and the Tier 1 (Award No: T1 251RES2207).

## References

- [1] Aioli, F. and Donini, M. (2015). Easymkl: a scalable multiple kernel learning algorithm. *Neurocomputing*, 169:215–224. Learning for Visual Semantic Understanding in Big Data ESANN 2014 Industrial Data Processing and Analysis.
- [2] Akian, J.-L., Bonnet, L., Owhadi, H., and Savin, E. (2022). Learning “best” kernels from data in Gaussian process regression. with application to aerodynamics. *Journal of Computational Physics*, 470:111595.
- [3] Alhusein, H., Khasawneh, M., and Daqaq, M. F. (2023). Physics-informed solution of the stationary fokker-plank equation for a class of nonlinear dynamical systems: An evaluation study. *arXiv preprint arXiv:2309.16725*.
- [4] Anderson, W. and Farazmand, M. (2023). Fisher information and shape-morphing modes for solving the Fokker-Planck equation in higher dimensions. *arXiv: 2306.03749*.
- [5] Baek, J. and Kim, E. (2019). A new support vector machine with an optimal additive kernel. *Neurocomputing*, 329:279–299.

- [6] Beck, C., Becker, S., Cheridito, P., Jentzen, A., and Neufeld, A. (2021). Deep splitting method for parabolic PDEs. *SIAM Journal on Scientific Computing*, 43(5):A3135–A3154.
- [7] Beck, C., E, W., and Jentzen, A. (2019). Machine learning approximation algorithms for high-dimensional fully nonlinear partial differential equations and second-order backward stochastic differential equations. *Journal of Nonlinear Science*, 29:1563–1619.
- [8] Beck, C., Hornung, F., Hutzenthaler, M., Jentzen, A., and Kruse, T. (2020). Overcoming the curse of dimensionality in the numerical approximation of Allen–Cahn partial differential equations via truncated full-history recursive multilevel Picard approximations. *Journal of Numerical Mathematics*, 28(4):197–222.
- [9] Becker, S., Cheridito, P., Jentzen, A., and Welti, T. (2021). Solving high-dimensional optimal stopping problems using deep learning. *European Journal of Applied Mathematics*, 32(3):470–514.
- [10] Boffi, N. M. and Vanden-Eijnden, E. (2023). Probability flow solution of the Fokker-Planck equation. *Machine Learning: Science and Technology*, 4(3):035012.
- [11] Chan-Wai-Nam, Q., Mikael, J., and Warin, X. (2019). Machine learning for semi linear pdes. *Journal of scientific computing*, 79(3):1667–1712.
- [12] Chen, Y., Owhadi, H., and Stuart, A. M. (2021). Consistency of empirical Bayes and kernel flow for hierarchical parameter estimation. *Math. Comp.*, 90(332):2527–2578.
- [13] Cho, J., Nam, S., Yang, H., Yun, S.-B., Hong, Y., and Park, E. (2022). Separable pinn: Mitigating the curse of dimensionality in physics-informed neural networks. *arXiv preprint arXiv:2211.08761*.
- [14] Dehghan, M. and Mohammadi, V. (2014). The numerical solution of Fokker-Planck equation with radial basis functions (RBFs) based on the meshless technique of kansa’s approach and Galerkin method. *Engineering Analysis with Boundary Elements*, 47:38–63.
- [15] Dobson, M., Li, Y., and Zhai, J. (2022). An efficient data-driven solver for Fokker-Planck equations: algorithm and analysis. *Commun. Math. Sci.*, 20(3):803–827.
- [16] E, W., Han, J., and Jentzen, A. (2021). Algorithms for solving high dimensional pdes: from nonlinear monte carlo to machine learning. *Nonlinearity*, 35(1):278.
- [17] Genz, A. (1984). Testing multidimensional integration routines. In *Proceedings of the International Conference on Tools, Methods and Languages for Scientific and Engineering Computation*, pages 81–94. Elsevier North-Holland, Amsterdam.
- [18] Gu, Y., Harlim, J., Liang, S., and Yang, H. (2023). Stationary density estimation of Itô diffusions using deep learning. *SIAM J. Numer. Anal.*, 61(1):45–82.
- [19] Hamzi, B. and Owhadi, H. (2021). Learning dynamical systems from data: a simple cross-validation perspective, part I: Parametric kernel flows. *Phys. D*, 421:Paper No. 132817, 10.
- [20] Han, J., Jentzen, A., and E, W. (2018). Solving high-dimensional partial differential equations using deep learning. *Proceedings of the National Academy of Sciences*, 115(34):8505–8510.
- [21] Han, J., Jentzen, A., et al. (2017). Deep learning-based numerical methods for high-dimensional parabolic partial differential equations and backward stochastic differential equations. *Communications in mathematics and statistics*, 5(4):349–380.



- [22] He, D., Li, S., Shi, W., Gao, X., Zhang, J., Bian, J., Wang, L., and Liu, T.-Y. (2023). Learning physics-informed neural networks without stacked back-propagation. In *International Conference on Artificial Intelligence and Statistics*, pages 3034–3047. PMLR.
- [23] Henry-Labordere, P. (2017). Deep primal-dual algorithm for bsdes: Applications of machine learning to cva and im. *Available at SSRN 3071506*.
- [24] Hu, Z., Shukla, K., Karniadakis, G. E., and Kawaguchi, K. (2023). Tackling the curse of dimensionality with physics-informed neural networks. *arXiv preprint arXiv:2307.12306*.
- [25] Huang, W., Ji, M., Liu, Z., and Yi, Y. (2015). Steady states of Fokker-Planck equations: I. Existence. *J. Dynam. Differential Equations*, 27(3-4):721–742.
- [26] Huré, C., Pham, H., and Warin, X. (2020). Deep backward schemes for high-dimensional nonlinear PDEs. *Mathematics of Computation*, 89(324):1547–1579.
- [27] Hutzenthaler, M., Jentzen, A., Kruse, T., Anh Nguyen, T., and von Wurstemberger, P. (2020). Overcoming the curse of dimensionality in the numerical approximation of semilinear parabolic partial differential equations. *Proceedings of the Royal Society A*, 476(2244):20190630.
- [28] Jain, A., Vishwanathan, S. V., and Varma, M. (2012). SPF-GMKL: generalized multiple kernel learning with a million kernels. In *Proceedings of the 18th ACM SIGKDD international conference on Knowledge discovery and data mining*, pages 750–758.
- [29] Ji, S., Peng, S., Peng, Y., and Zhang, X. (2020). Three algorithms for solving high-dimensional fully coupled FBSDEs through deep learning. *IEEE Intelligent Systems*, 35(3):71–84.
- [30] Jordan, R., Kinderlehrer, D., and Otto, F. (1998). The variational formulation of the Fokker-Planck equation. *SIAM J. Math. Anal.*, 29(1):1–17.
- [31] Karniadakis, G. E., Kevrekidis, I. G., Lu, L., Perdikaris, P., Wang, S., and Yang, L. (2021). Physics-informed machine learning. *Nature Reviews Physics*, 3(6):422–440.
- [32] Kazem, S., Rad, J., and Parand, K. (2012). Radial basis functions methods for solving Fokker-Planck equation. *Engineering Analysis with Boundary Elements*, 36(2):181–189.
- [33] Kingma, D. P. and Ba, J. (2015). Adam: A method for stochastic optimization. *ICLR*.
- [34] Kloft, M., Brefeld, U., Sonnenburg, S., and Zien, A. (2011). Lp-norm multiple kernel learning. *The Journal of Machine Learning Research*, 12:953–997.
- [35] Lagaris, I., Likas, A., and Papageorgiou, D. (2000). Neural-network methods for boundary value problems with irregular boundaries. *IEEE Transactions on Neural Networks*, 11(5):1041–1049.
- [36] Li, Y. and Meredith, C. (2023). Artificial neural network solver for time-dependent Fokker-Planck equations. *Appl. Math. Comput.*, 457:Paper No. 128185, 24.
- [37] Lin, B., Li, Q., and Ren, W. (2022). Computing the invariant distribution of randomly perturbed dynamical systems using deep learning. *J. Sci. Comput.*, 91(3):Paper No. 77, 17.
- [38] Lin, B., Li, Q., and Ren, W. (2023). Computing high-dimensional invariant distributions from noisy data. *J. Comput. Phys.*, 474:Paper No. 111783, 16.

- [39] Liu, S., Li, W., Zha, H., and Zhou, H. (2022). Neural parametric fokker–planck equation. *SIAM Journal on Numerical Analysis*, 60(3):1385–1449.
- [40] Mandal, P. and Apte, A. (2023). Learning zeros of Fokker-Planck operators. *arXiv:2306.07068*.
- [41] Mishra, P. K., Fasshauer, G. E., Sen, M. K., and Ling, L. (2019). A stabilized radial basis-finite difference (RBF-FD) method with hybrid kernels. *Comput. Math. Appl.*, 77(9):2354–2368.
- [42] Mishra, P. K., Nath, S. K., Sen, M. K., and Fasshauer, G. E. (2018). Hybrid Gaussian-cubic radial basis functions for scattered data interpolation. *Comput. Geosci.*, 22(5):1203–1218.
- [43] Moeller, J., Raman, P., Venkatasubramanian, S., and Saha, A. (2014). A geometric algorithm for scalable multiple kernel learning. In *Artificial Intelligence and Statistics*, pages 633–642. PMLR.
- [44] Nguyen, T. M., Pham, M., Nguyen, T. M., Nguyen, K., Osher, S., and Ho, N. (2022). Fourierformer: Transformer meets generalized Fourier integral theorem. In Oh, A. H., Agarwal, A., Belgrave, D., and Cho, K., editors, *Advances in Neural Information Processing Systems*.
- [45] Orabona, F. and Luo, J. (2011). Ultra-fast optimization algorithm for sparse multi kernel learning. In *Proceedings of the 28th International Conference on Machine Learning*, number CONF.
- [46] Owhadi, H. and Yoo, G. R. (2019a). Kernel flows: from learning kernels from data into the abyss. *J. Comput. Phys.*, 389:22–47.
- [47] Owhadi, H. and Yoo, G. R. (2019b). Kernel flows: From learning kernels from data into the abyss. *Journal of Computational Physics*, 389:22–47.
- [48] Raissi, M. (2018). Forward-backward stochastic neural networks: Deep learning of high-dimensional partial differential equations. *arXiv preprint arXiv:1804.07010*.
- [49] Raissi, M., Perdikaris, P., and Karniadakis, G. E. (2019). Physics-informed neural networks: A deep learning framework for solving forward and inverse problems involving nonlinear partial differential equations. *Journal of Computational Physics*, 378:686–707.
- [50] Rakotomamonjy, A., Bach, F. R., Canu, S., and Grandvalet, Y. (2008). Simplemkl. *Journal of Machine Learning Research*, 9(83):2491–2521.
- [Risken] Risken, H. *The Fokker-Planck equation*, volume 18 of *Springer Series in Synergetics*. Springer-Verlag, Berlin, 2nd edition. Methods of solution and applications.
- [52] Senel, C. B., van Beeck, J., and Altinkaynak, A. (2022). Solving PDEs with a hybrid radial basis function: power-generalized multiquadric kernel. *Adv. Appl. Math. Mech.*, 14(5):1161–1180.
- [53] Sonnenburg, S., Rätsch, G., Schäfer, C., and Schölkopf, B. (2006). Large scale multiple kernel learning. *The Journal of Machine Learning Research*, 7:1531–1565.
- [54] Tabandeh, A., Sharma, N., Iannacone, L., and Gardoni, P. (2022). Numerical solution of the Fokker-Planck equation using physics-based mixture models. *Computer Methods in Applied Mechanics and Engineering*, 399:115424.

- [55] Tang, K., Wan, X., and Liao, Q. (2022). Adaptive deep density approximation for Fokker-Planck equations. *J. Comput. Phys.*, 457:Paper No. 111080, 19.
- [56] Varma, M. and Babu, B. R. (2009). More generality in efficient multiple kernel learning. In *Proceedings of the 26th annual international conference on machine learning*, pages 1065–1072.
- [57] Wang, X., Jiang, J., Hong, L., Zhao, A., and Sun, J.-Q. (2023). Radial basis function neural networks solution for stationary probability density function of nonlinear stochastic systems. *Probabilistic Engineering Mechanics*, 71:103408.
- [58] Wang, Y., Jin, P., and Xie, H. (2022a). Tensor neural network and its numerical integration. *arXiv preprint arXiv:2207.02754*.
- [59] Wang, Y., Liao, Y., and Xie, H. (2022b). Solving schrödinger equation using tensor neural network. *arXiv preprint arXiv:2209.12572*.
- [60] Yang, L., Sun, X., Hamzi, B., Owhadi, H., and Xie, N. (2024). Learning dynamical systems from data: A simple cross-validation perspective, part v: Sparse kernel flows for 132 chaotic dynamical systems. *Physica D: Nonlinear Phenomena*, page 134070.
- [61] Yoo, G. R. and Owhadi, H. (2021). Deep regularization and direct training of the inner layers of neural networks with kernel flows. *Phys. D*, 426:Paper No. 132952, 7.
- [62] Zhai, J., Dobson, M., and Li, Y. (2022). A deep learning method for solving Fokker-Planck equations. In Bruna, J., Hesthaven, J., and Zdeborova, L., editors, *Proceedings of the 2nd Mathematical and Scientific Machine Learning Conference*, volume 145 of *Proceedings of Machine Learning Research*, pages 568–597. PMLR.
- [63] Zhang, H., Xu, Y., Liu, Q., and Li, Y. (2023). Deep learning framework for solving Fokker-Planck equations with low-rank separation representation. *Engineering Applications of Artificial Intelligence*, 121:106036.
- [64] Zhang, H., Zhang, R., and Zhou, T. (2022). A predictor-corrector deep learning algorithm for high dimensional stochastic partial differential equations. *arXiv:2208.09883*.

## A Universal approximation of tensor neural networks

We use a similar argument in [44] to show the universal approximation property of tensor neural networks. Recall from the Fourier integral theorem, for any  $p(x) \in L^1(\mathbb{R}^d)$ ,

$$p(x) = \frac{1}{(2\pi)^d} \int_{\mathbb{R}^d} \int_{\mathbb{R}^d} \cos(z^\top(x-y)) p(y) dz dy$$

Observe that

$$\int_{\mathbb{R}^d} \cos(z^\top(x-y)) dz = \lim_{R \rightarrow \infty} \int_{[-R,R]^d} \cos(z^\top(x-y)) dz = \lim_{R \rightarrow \infty} \prod_{j=1}^d \frac{\sin(R(x_j - y_j))}{(x_j - y_j)}.$$

We then approximate the integral

$$p(x) = \lim_{R \rightarrow \infty} \frac{1}{(2\pi)^d} \int_{[-R,R]^d} \mathcal{K}_R(x-y) p(y) dy, \quad \mathcal{K}_R(x-y) = \prod_{j=1}^d \frac{\sin(R(x_j - y_j))}{(x_j - y_j)} = \prod_{j=1}^d K_{R,j}(x_j - y_j).$$

Specifically, we have the error  $\varepsilon_R$  from approximating the whole space with  $[-R, R]^d$  and the error  $\varepsilon_{\text{int}}$  of numerical integration over this bounded domain.

$$p(x) = \int_{[-R, R]^d} \mathcal{K}_R(x - y)p(y) dy + \varepsilon_R = \sum_{|\alpha|=1}^N c_\alpha \prod_{j=1}^d K_{R,j}(x_j - y_{j,\alpha_i}) + \varepsilon_{\text{int}} + \varepsilon_R.$$

Here  $y_{j,\alpha_i}$  are sampling points along the direction  $y_j$  and  $c_\alpha$  depends on  $p(y)$  and  $y_{j,\alpha_i}$ . The numerical integration can be realized by the Monte Carlo method when  $p(y)$  is continuous on  $[-R, R]^d$  and has second-order moments. This shows a universal approximation of the tensor-product kernels. Observe that the kernel in each dimension is continuous and thus can be approximated by another kernel function or neural network with universal approximation property in each dimension.